European Cells and Materials Vol.57 2026 (pages 181–198) DOI: 10.22203/eCM.v057a09 ISSN 1473-2262

Original Article

COMBINED PHOTOTHERMAL ABLATION AND ANTI-INFLAMMATION USING ROS-RESPONSIVE METAL-POLYPHENOL NANOPLATFORM FOR PRECISION THERAPY OF ENDOMETRIOSIS

Xiao Zhou[1], Yisha Zheng[1], Danhong Hu[1] and Jingwei Hu[2,*]

[1]Department of Obstetrics, The Second Affiliated Hospital and Yuying Children's Hospital of Wenzhou Medical University, 325027 Wenzhou, Zhejiang, China

[2]Department of Surgery, The Second Affiliated Hospital and Yuying Children's Hospital of Wenzhou Medical University, 325027 Wenzhou, Zhejiang, China

Abstract

Background: Endometriosis (EMs) is a prevalent gynecological inflammatory disorder characterized by ectopic endometrial tissue growth and a high-ROS microenvironment. In this study, mesoporous silica ($mSiO_2$) was employed to load the COX2 inhibitor celecoxib (CXB), followed by Fe^{3+}-epigallocatechin gallate (EGCG) self-assembly to form a metal-polyphenol coating. The efficacy and biosafety of the resulting nanoparticles (SC@FEG) combined with photothermal therapy (PTT) were systematically investigated, aiming to achieve precise treatment for EMs. **Methods**: SC@FEG was characterized by dynamic light scattering (DLS), transmission electron microscopy (TEM), and UV-visible spectroscopy, and its ROS-responsive release and photothermal performance were examined. In ectopic endometrial stromal cells (eESCs), the effects of SC@FEG combined with near-infrared (NIR) irradiation were assessed via CCK-8, Calcein-AM/PI staining, Transwell assays, and Western blotting. Moreover, an EMs mouse model was established, and lesion-targeted accumulation and heating effects were monitored by infrared thermography. Apoptosis and fibrosis of ectopic lesions were examined by TUNEL and Masson staining, while anti-inflammatory efficacy was evaluated by Western blotting and ELISA. Biosafety was further assessed by hemolysis testing, histology, and serum biochemistry. **Results**: SC@FEG displayed stable physicochemical properties, efficient ROS-responsive release, and excellent photothermal conversion. *In vitro*, SC@FEG with NIR irradiation markedly suppressed eESCs' proliferation, migration, and invasion, while reducing COX2 expression. *In vivo*, SC@FEG accumulated in lesions, induced local hyperthermia under laser irradiation, inhibited lesion growth, promoted apoptosis, alleviated fibrosis, and markedly reduced systemic inflammation, without systemic toxicity. **Conclusions**: SC@FEG represents a multifunctional nanoplatform that combines photothermal ablation and anti-inflammatory drug delivery, providing safe and precise therapy for EMs.

Keywords: Endometriosis, cyclooxygenase-2, celecoxib, ROS sensitive, photothermal therapy.

***Address for correspondence**: Jingwei Hu, Department of Surgery, The Second Affiliated Hospital and Yuying Children's Hospital of Wenzhou Medical University, 325027 Wenzhou, Zhejiang, China. E-mail: hjwmed@163.com.

Introduction

Endometriosis (EMs) is a prevalent gynecological disorder characterized by estrogen-dependent inflammatory responses, affecting approximately 10%-15% of women of reproductive age worldwide [1]. Its clinical manifestations include progressively aggravated dysmenorrhea, chronic pelvic pain, and infertility, which severely compromise patients' quality of life and reproductive health [2,3]. The principal pathological feature of EMs is the abnormal colonization of endometrium-like tissue outside the uterine cavity, accompanied by elevated local oxidative stress, persistent inflammatory activation, and excessive neovascularization at the lesion sites. These factors not only promote the growth and invasion of ectopic endometrial tissue but also further exacerbate pain and disease progression [4]. Currently, clinical management strategies for EMs primarily encompass pharmacological therapy and surgical intervention. However, existing pharmacological treatments depend on hormone suppression, often accompanied by substantial side effects, and fail to eradicate the disease, while surgery entails significant invasiveness and a high recurrence rate [5]. Consequently, there is an urgent need for novel therapeutic strategies capable of precisely target-

ing the complex pathological microenvironment of EMs and achieving combinatorial therapy with multiple mechanisms, thereby improving the prognosis of EMs patients.

Sustained activation of inflammatory responses constitutes one of the central mechanisms driving the progression of EMs, in which cyclooxygenase-2 (COX2), a critical rate-limiting enzyme in the inflammatory cascade, is markedly overexpressed in ectopic lesion tissues of EMs [6]. By catalyzing the conversion of arachidonic acid into inflammatory mediators such as prostaglandin E2 (PGE_2), COX2 not only intensifies local inflammatory infiltration and pain but also accelerates neovascularization in ectopic lesions by promoting the release of vascular endothelial growth factor (VEGF), thereby facilitating the abnormal colonization and invasion of endometrial tissue [7]. Presently, nonsteroidal anti-inflammatory drugs (NSAIDs), as classic COX inhibitors, are the first-line agents for managing EMs-associated pain [8]. Among them, celecoxib (CXB) has been demonstrated to specifically block COX2-mediated inflammatory pathways, effectively reducing PGE_2 production in EMs lesions, alleviating chronic pelvic pain, and suppressing the proliferation of ectopic endometrial cells and angiogenesis [8]. Nevertheless, conventional administration of CXB is hindered by poor solubility, low bioavailability, lack of lesion-specific targeting, and potential gastrointestinal and cardiovascular adverse events upon long-term systemic administration [9], thereby limiting its widespread application in EMs treatment. Hence, the development of a novel delivery system capable of achieving specific drug release against the highly reactive oxygen species (ROS) microenvironment of EMs lesions, which can improve the enrichment and release efficiency of CXB at the lesion site as well as reduce its systemic toxicity, is of great significance in improving the efficacy and safety of CXB in EMs therapy.

In recent years, rapid advances in materials science and intelligent drug delivery technologies have driven the rise of nano-delivery systems as promising solutions to overcome the limitations of conventional drug administration and achieve precise targeted therapy [10]. Among various nanocarriers, mesoporous silica ($mSiO_2$) stands out due to its high specific surface area, tunable pore structure, and excellent biocompatibility, making it an ideal platform for efficient drug loading and controlled release [11]. To further endow nanocarriers with microenvironment-responsive properties and additional therapeutic functions, surface engineering strategies have been extensively explored. Metal-phenolic networks (MPNs) represent a class of emerging multifunctional nano-coating materials that harness the coordination interactions between polyphenols and metal ions to generate robustly adherent and stimuli-responsive layers [12]. Of particular relevance, epigallocatechin gallate (EGCG), a natural polyphenol with anti-inflammatory, antibacterial, and anti-infective properties, can self-assemble with Fe^{3+} to form a stable Fe^{3+}-EGCG coating (FEG) [13]. Importantly, this coating enables the nanosystem to achieve ROS-responsive drug release in the microenvironment of EMs lesions, while simultaneously conferring efficient photothermal conversion capability [14]. Given the superficial distribution, accessibility, and invasive growth characteristics of ectopic lesions, localized hyperthermia enables precise lesion ablation while minimizing damage to surrounding normal tissue [15], suggesting that leveraging the photothermal properties for photothermal therapy (PTT) represents a rational and promising strategy for EMs treatment. As a minimally invasive modality, PTT relies on photothermal conversion materials to generate local hyperthermia under NIR irradiation for selective lesion ablation [16]. Although EMs is a benign disease, the invasive growth, ectopic dissemination, and recurrent relapse of endometrial lesions render conventional surgical or pharmacological interventions often insufficient for durable efficacy [17]. Therefore, combining PTT with anti-inflammatory drug delivery is expected to achieve both inflammation suppression and thermal ablation of lesions, avoiding surgical trauma and high recurrence risks, and providing an efficient and precise combinatorial therapeutic strategy for EMs.

Based on this rationale, the present study constructed a nanosystem in which $mSiO_2$ served as the drug carrier for CXB, while coordination-driven self-assembly of Fe^{3+} with EGCG generated an MPN that sealed CXB within the mesopores of $mSiO_2$, ultimately yielding $mSiO_2$-CXB@Fe^{3+}-EGCG nanoparticles (SC@FEG) with both ROS-responsive and photothermal conversion capabilities. By systematically evaluating the therapeutic efficacy and biosafety of SC@FEG in combination with PTT for EMs, this study aims to provide experimental evidence for the clinical development of an innovative precision-targeted therapeutic strategy.

Materials and Methods

Preparation of S@FEG and SC@FEG

First, 0.5 g of cetyltrimethylammonium chloride (CTAC) and 0.06 g of triethanolamine (TEA) were dissolved in 20 mL of deionized water and stirred at 80 °C for 20 minutes to obtain solution A. Subsequently, 1 mL of tetraethyl orthosilicate (TEOS) and 0.2 mL of bis-(γ-triethoxysilylpropyl)-tetrasulfide (BTES) were mixed and sonicated for 30 minutes to yield solution B. Solution B was then slowly added dropwise into solution A and the mixture was stirred continuously at 80 °C for 4 h. The resulting product was collected by centrifugation (12,000 rpm, 20 min) and washed with anhydrous ethanol to remove unreacted impurities. To eliminate the CTAC template, the obtained white precipitate was dispersed in 20 mL of NaCl-methanol solution and stirred for 12 h. The precipitate was recollected by centrifugation (10,000 rpm, 10 min), washed three times with anhydrous ethanol, and vacuum-dried at 60 °C, yielding $mSiO_2$.

To prepare $mSiO_2$-CXB (SC) nanoparticles, 6 mg of CXB was loaded into the mesopores of $mSiO_2$. Specifically, 5 mL of $mSiO_2$ solution (10 mg/mL) was mixed with 2 mL of CXB ethanol solution (3 mg/mL) and stirred for 24 hours to ensure sufficient loading of the drug into the pores of $mSiO_2$. The precipitate was harvested by centrifugation (12,000 rpm, 20 min) and washed three times with deionized water, resulting in SC nanoparticles.

The supernatants were collected immediately following centrifugation, and the amount of free CXB was quantified using high-performance liquid chromatography (HPLC). HPLC was performed using an Eclipse XBD-C18 column (4.6 × 250 mm, 5 μm) at 25 °C. The mobile phase was a mixture of 0.02 M potassium dihydrogen phosphate buffer (pH 5.8) and acetonitrile (45: 55, v/v) at a flow rate of 1.0 mL/min. The detection wavelength was set at 252 nm, and the injection volume was 10 μL. The encapsulation efficiency (EE%) and drug loading capacity (LC%) were calculated according to the following equations:

$$EE(\%) = \frac{W_{total} - W_{free}}{W_{total}} \times 100\% \quad (1)$$

$$LC(\%) = \frac{W_{total} - W_{free}}{M} \times 100\% \quad (2)$$

Where W_{total} represents the total amount of CXB initially added, W_{free} denotes the amount of unencapsulated CXB in the supernatant, and M refers to the total mass of SC nanoparticles.

Furthermore, the FEG coating was applied to SC to prepare SC@FEG nanoparticles with both photothermal conversion properties and ROS responsiveness. EGCG solution (500 μL, 10 mM) and $FeCl_3 \cdot 6H_2O$ solution (100 μL, 50 mM) were sequentially added to SC solution (5 mL, 1 mg/mL) under stirring. After ultrasonic vortexing for 30 s, the pH was adjusted to 8.0 with 0.1 M NaOH solution, and stirring was continued for 20 min. The resulting product was collected by centrifugation (12,000 rpm, 20 min) and washed three times with deionized water to obtain SC@FEG nanoparticles. In parallel, the drug-free $mSiO_2$ solution was subjected to the same coating procedure to generate $mSiO_2$@Fe^{3+}-EGCG (S@FEG) nanoparticles, which preserved the core physicochemical and functional properties and were used for subsequent control studies.

Characterization of Physicochemical Properties of SC@FEG

Dynamic light scattering (DLS) was employed to determine the hydrodynamic size distribution, polydispersity index (PDI), and ζ-potential of $mSiO_2$, SC, and SC@FEG, with each sample analyzed in triplicate. Transmission electron microscopy (TEM) was used to observe the microstructure and morphological characteristics of $mSiO_2$ and SC@FEG, with $mSiO_2$ and SC@FEG deposited onto carbon-coated copper grids and vacuum-dried before imaging. Ultraviolet-visible (UV-Vis) spectroscopy was conducted to detect the characteristic absorption peaks of $mSiO_2$, CXB, $FeCl_3$, EGCG, and SC@FEG, to verify the successful incorporation of each component. Fourier-transform infrared (FTIR) spectroscopy was employed to characterize the chemical bonds and functional groups of $mSiO_2$, CXB, EGCG, and SC@FEG, so as to confirm the coordination interaction between Fe^{3+} and EGCG and the successful encapsulation of CXB. To further evaluate the stability, SC@FEG was dispersed in DMEM medium and deionized water, and changes in particle size were monitored by DLS daily for 14 days.

In Vitro Drug Release Studies

The SC@FEG solution was placed in a dialysis bag (molecular weight cutoff: 3500 Da), which was then immersed in 20 mL of release medium, either PBS (pH 7.4, containing 1% v/v Tween-80) or PBS simulating oxidative stress conditions (containing 1% v/v Tween-80 with 0.05, 0.1, 0.5, and 1 mM H_2O_2), as reported in previous EMs studies [18]. The release experiment was conducted in a shaker at 37 °C with a rotation speed of 100 rpm. At each preset time point (1, 2, 4, 8, 12, 24, 36, 48 h), 1 mL of release medium was withdrawn and immediately replaced with an equal volume of fresh medium at the same temperature. The concentration of CXB in the release solution was detected by high-performance liquid chromatography (HPLC), and the cumulative drug release amount was calculated according to the following formula:

$$S(\%) = \frac{\sum_{i=1}^{n-1} V_a C_i + V_0 C_n}{M} \times 100\% \quad (3)$$

Where V_0 represents the initial total volume of the release medium (20 mL), V_a denotes the volume of each sample taken (1 mL), Cn is the concentration of CXB in the release medium at the nth sampling, and M is the total amount of CXB encapsulated in SC@FEG. By comparing the drug release curves in different release media, the controlled drug release behavior of SC@FEG under physiological conditions and oxidative stress microenvironment was evaluated.

Detection of the Photothermal Performance of SC@FEG

To systematically evaluate the photothermal performance of SC@FEG, temperature changes under different conditions were monitored by adjusting its concentration (0, 50, 100, 150, 200 μg/mL) and laser irradiation power (0.5, 1, 1.5, 2, 2.5 W/cm^2). To further investigate its photothermal stability, the sample was irradiated with a laser

for 500 s, after which the irradiation was stopped, and the sample was allowed to cool naturally to the initial temperature. This heating and cooling process was cycled five times, and temperature changes were recorded in real time. A temperature-time curve was plotted to reflect its photothermal stability. In addition, the photothermal conversion efficiency (η) of SC@FEG was calculated using the following formula:

$$\eta = \frac{hs(Tmax - Ts) - Q_{Dis}}{I(1 - 10^{-A})} \quad (4)$$

Where h represents the heat transfer coefficient, s is the surface area of the container, T_{max} is the maximum temperature, T_s is the room temperature, I is the laser power, A is the absorbance of the dispersion at 808 nm, and Q_{Dis} is the heat absorbed and dissipated by the solvent and the container.

To visualize the time-dependent photothermal behavior of SC@FEG, infrared thermal images were captured under NIR irradiation (808 nm, 1.5 W/cm^2) at 0, 1, 2, 3, 4, 5, and 6 minutes, and the temperature variations were recorded in real time.

Establishment of the Mouse Model of EMs

Female C57BL/6J mice (6–8 weeks old, 16–24 g) were purchased from Sipeifu Biotechnology Co., Ltd. (Beijing, China) for the construction of the EMs mice model. All mice were housed under specific pathogen-free (SPF) conditions with controlled relative humidity of 60–65%, temperature of 23 ± 2 °C, and a 12-hour light/dark cycle, with free access to standard chow and water. All experimental procedures were approved by the Laboratory Animal Management and Ethics Committee of Wenzhou Medical University (approval No.: wydw-2025-0463) and were strictly performed in accordance with the Guidelines for Ethical Review of Laboratory Animal Welfare and relevant regulations.

The EMs mouse model was established by autologous endometrial transplantation [19]. Specifically, mice were anesthetized by isoflurane inhalation (3% for induction, 1.3% for maintenance). Under sterile conditions, the middle segment of the right uterine horn was excised and immediately placed in DMEM/F12 medium. The uterine horn tissue was longitudinally incised and trimmed into 5 × 5 mm fragments, which were then placed with the endometrial surface facing the inner abdominal wall and fixed onto the right abdominal wall of the mice using sterile sutures. Thereafter, the abdominal muscles and skin were sutured layer by layer to complete the operation. Postoperatively, penicillin (20,000 U/mouse) was intraperitoneally administered once daily for three consecutive days to prevent infection. To mimic the *in vivo* estrogenic microenvironment and promote the growth of ectopic endometrial tissue, 1 mg/mL estradiol solution (20 μL/mouse) was subcutaneously injected every 5 days postoperatively, with a total of 4 injections. At 21 days post-surgery, 3 mice were randomly selected for reopening of the abdomen to observe the morphology of ectopic lesions and to excise the lesion tissues. Histological examination was performed to confirm the formation of ectopic endometrial glands and stromal structures, ensuring the successful establishment of the model. The remaining mice were used for subsequent experiments.

Isolation of Ectopic Endometrial Stromal Cells (eESCs)

The eESCs were isolated from the EMs mouse model according to the method reported in previous literature [18]. Specifically, the model mice were sacrificed, and the ectopic endometrial tissues were aseptically obtained from the lesions. The tissues were cut into 1–2 mm fragments and incubated in DMEM/F12 medium containing 1 mg/mL collagenase type IV at 37 °C with agitation for 20 min. After digestion, the dispersed cells were separated using a 400-mesh cell strainer, while the large tissue pieces that did not pass through the strainer were subjected to repeated digestion for another 20 minutes and secondary filtration to maximize cell yield. The digested cells were collected and centrifuged at 1500 rpm for 10 min, and the supernatant was discarded. The cells were resuspended and washed with DMEM/F12 medium supplemented with 10% fetal bovine serum (FBS) and 1% penicillin-streptomycin. Then, the cell suspension was seeded into culture dishes and incubated overnight in a 37 °C, 5% CO_2 incubator. On the following day, non-adherent cells were removed by rinsing with PBS 2–3 times. Prior to subsequent experiments, mycoplasma contamination was excluded using a commercial detection kit according to the manufacturer's instructions. In addition, to verify cell purity and identity, immunofluorescence staining for vimentin (stromal cell marker) and cytokeratin (epithelial cell marker), as well as flow cytometry analysis for CD45, CD90, and CD105, were carried out. Cells with positive expression of vimentin and negative expression of cytokeratin, as well as the $CD45^-CD90^+$ and $CD45^-CD105^+$ populations, were identified as eESCs. After purity validation, cells that reached 90% confluence were digested with trypsin and passaged for subsequent experiments.

Cell Counting Kit-8 (CCK-8)

eESCs in the logarithmic growth phase were seeded into 96-well plates and cultured routinely until they adhered to the plate, after which different treatments were administered. To evaluate concentration-dependent cytotoxicity, the eESCs were exposed to free CXB at varying concentrations (0, 10, 20, 40, 80, and 160 μM) for 24 h. For group comparisons, the cells were divided into four groups: control, free CXB, S@FEG, and SC@FEG, with each group further subdivided into NIR (−) and NIR (+) subgroups. In

the NIR (+) subgroups, following 24 hours of co-incubation of drugs with cells, the cells were irradiated with an 808 nm NIR laser (1.5 W/cm^2) for 5 min. At the end of the treatment, 10 μL of CCK-8 solution was added to each well, and the plates were incubated at 37 °C for 2 h. Absorbance at 450 nm was measured using a microplate reader (BioTek, USA), and relative cell viability was calculated to assess the effects of different treatments on eESCs proliferation.

Live/Dead Cell Staining

eESCs in the logarithmic growth phase were seeded into 6-well plates. After the cells adhered and the corresponding treatments were completed, the culture medium was discarded, and the cells were gently washed twice with PBS buffer. A pre-prepared Calcein-AM/PI double-staining reagent was then added, followed by incubation in the dark for 30 min. After incubation, the cells were rinsed three times with PBS to remove unbound dyes and then immediately observed and imaged under a fluorescence microscope. Live cells labeled with Calcein-AM exhibited green fluorescence, while dead cells labeled with PI showed red fluorescence. The effects of each treatment on cell survival status were visually evaluated by comparing the relative proportions and distributions of green and red fluorescent areas among different treatment groups.

Transwell Assay

Transwell chambers were used to assess the effects of different treatments on the migration and invasion abilities of eESCs. For the migration assay, 200 μL of eESCs suspended in serum-free medium (approximately 5×10^4 cells) was first added to the upper chamber, and 600 μL of medium containing 10% FBS was added to the lower chamber as a chemoattractant. For the invasion assay, Matrigel (BD Biosciences, USA) was evenly spread on the surface of the upper chamber membrane in advance and incubated at 37 °C for 2 h, after which approximately 5×10^4 cells were seeded into the upper chamber. All chambers were incubated in a 37 °C, 5% CO_2 incubator for 24 hours (48 hours for the invasion assay). At the end of incubation, non-migrated or non-invaded cells in the upper chamber were gently wiped off with cotton swabs. The chambers were then washed with PBS, fixed with 4% paraformaldehyde for 20 min, and stained with 0.1% crystal violet for 30 min. Finally, three random fields of view were photographed and counted under a microscope to calculate the proportion of migrated or invaded cells.

Western Blot

eESCs or ectopic lesion tissues from EMs model mice were lysed in RIPA lysis buffer containing PMSF. After incubation on ice for 30 min, the lysate was centrifuged at 12,000 rpm for 15 min, and the supernatant was collected to obtain total protein. The protein concentration was determined by the BCA method, and an aliquot of the protein sample was separated by electrophoresis on 10% SDS-PAGE gels, followed by transferring the protein to the PVDF membrane. The membranes were blocked in TBST buffer containing 5% non-fat milk powder at room temperature for 1 h, and then incubated with primary antibodies (anti-COX2, 1:1000, CST; β-actin, 1:5000, Proteintech) at 4 °C overnight. After washing the membranes, they were incubated with HRP-labeled secondary antibodies for 1 hour and then washed three times with TBST. Finally, an ECL luminescence kit was utilized for development, and band signals were acquired using a chemiluminescence imaging system. The grayscale values of the protein bands were analyzed with ImageJ software, and the expression level of COX2 was normalized using β-actin as the internal reference.

Enzyme-Linked Immunosorbent Assay (ELISA)

Commercially available ELISA kits were used to determine the levels of PGE_2, TNF-α, IL-6, and IL-1β in the culture supernatants of eESCs and mouse serum samples according to the manufacturer's instructions. The absorbance was measured at a wavelength of 450 nm using a microplate reader, and the concentration of each cytokine was calculated via the standard curve.

In Vivo Fluorescence Imaging

To determine the optimal time window for NIR irradiation, IR780-loaded nanoparticles (SI@FEG) were prepared, with IR780 being the fluorescent tracer. Female EMs model mice were intravenously injected with SI@FEG or free IR780. At predetermined time points post-injection (1, 3, 6, 12, 24 h), the fluorescence distribution was monitored using an *in vivo* imaging system (IVIS).

Grouping and Treatment of EMs Model Mice

Twenty-one days after modeling and successful model verification, the mice were randomly divided into 6 groups (n = 5): PBS group (control), CXB group, S@FEG group, S@FEG+NIR group, SC@FEG group, and SC@FEG+NIR group. An equal volume of drug was injected through the tail vein, and the drug dose was calculated based on the CXB equivalent concentration of 5 mg/kg, whereas the dose administered in the S@FEG group was set according to the mass equivalence of the carrier ($mSiO_2$@Fe^{3+}-EGCG) in the SC@FEG group to exclude interference from the carrier itself.

Based on the results of *in vivo* fluorescence imaging, the ectopic lesions of the S@FEG+NIR group and SC@FEG+NIR group were accurately irradiated with an 808 nm NIR laser (power density 1.5 W/cm^2, irradiation time 3 min) at 6 hours after drug administration. All experimental groups received tail vein injections once every 48 hours for a total of eight administrations, during which body weight changes of the mice were continuously monitored and recorded.

In Vivo Real-Time Photothermal Imaging

An infrared thermal imager was employed to monitor and record the temperature changes of the lesion area in mice at different time points (0, 0.5, 1, 2, 3, 5 min) during the irradiation process. Thermal images and corresponding temperature values at each time point were acquired to evaluate the *in vivo* photothermal heating effect of SC@FEG.

Immunofluorescence and Histological Staining

Ectopic lesion tissues from EMs mice, as well as major organ tissues (including ovary, uterus, heart, liver, spleen, lung, and kidney) from the mice in the PBS and SC@FEG+NIR groups, were collected. After fixation with 4% paraformaldehyde, tissues underwent routine paraffin embedding and sectioning (approximately 4 μm thick). The sections were baked at 60 °C, dewaxed with xylene, and hydrated with gradient ethanol for subsequent use.

TUNEL staining was performed to detect cell apoptosis in ectopic lesions, and apoptotic cells showed green fluorescent signals under a fluorescence microscope. Masson's trichrome staining was used to evaluate the degree of fibrosis in ectopic lesion tissues, with collagen fibers stained blue. Hematoxylin and eosin (H&E) staining was applied to observe the overall pathological changes of major organs, and the tissue structure and morphological characteristics were examined under a light microscope.

Hemolysis Assay

Fresh mouse blood was treated with an anticoagulant and mixed with 10 mL of PBS, followed by centrifugation at 2000 rpm for 10 minutes. The supernatant was discarded, and the red blood cell (RBC) precipitate was collected. RBCs were gently resuspended and washed with physiological saline, centrifuged at 2000 rpm for 10 minutes, and this washing process was repeated three times until the supernatant became clear and transparent. The collected RBCs were added to 10 mL of PBS to form a cell suspension.

Subsequently, 200 μL of the RBC suspension was added to Eppendorf tubes containing 800 μL of SC@FEG at different concentrations (50, 100, 200, and 400 μg/mL), 800 μL of PBS (negative control), and 800 μL of Triton X-100 (positive control), respectively. After mixing with gentle shaking, each Eppendorf tube was irradiated with an NIR laser (808 nm, 1.5 W/cm^2) for 3 minutes, and then incubated at 37 °C for 1 hour, followed by centrifugation at 3000 rpm for 5 minutes. The supernatant was taken at 540 nm to determine the absorbance value and calculate the hemolysis rate, and the hemolysis rate $<$5% was used to determine that the nanoparticles had good hemocompatibility [20].

Biochemical Detection

Mouse serum was left at room temperature for approximately 2 hours until stratification, then centrifuged at 2000 $\times$ g for 20 minutes. The supernatant was then carefully collected and aliquoted into a 1.5 mL centrifuge tube, with the aliquot of serum mixed thoroughly with sterile 1$\times$PBS solution in a 1:3 ratio. Biochemical indices, including red blood cells (RBC), white blood cells (WBC), platelets (PLT), hemoglobin (HGB), alanine aminotransferase (ALT), aspartate aminotransferase (AST), creatine kinase (CK), and lactate dehydrogenase (LDH), were measured using a Hitachi 3100 automatic biochemical analyzer.

Statistical Analysis

All statistical analyses were performed using GraphPad Prism 9.0 (San Diego, California, USA). Data were expressed as mean $\pm$ standard deviation (Mean $\pm$ SD). Comparisons among multiple groups were performed using one-way analysis of variance (ANOVA). When significant differences were identified, post-hoc tests were used for pairwise comparisons. For comparisons between two groups, the unpaired Student's t-test was used for normally distributed data, and the Mann-Whitney U test was used for non-normally distributed data. A p-value less than 0.05 was considered statistically significant.

Results

Characterization of the Physicochemical Properties of SC@FEG

To address the issues of insufficient targeting and restricted efficacy of CXB in EMs treatment, this study designed and synthesized SC@FEG, a ROS-responsive nanoplatform with dual photothermal conversion and anti-inflammatory functions, and systematically characterized its physicochemical properties. DLS results revealed that the average particle size of $mSiO_2$ was 127.8 $\pm$ 5.41 nm (Fig. 1**A**), which increased to 138.21 $\pm$ 1.49 nm following CXB loading (Fig. 1**B**), and further expanded to 144.3 $\pm$ 6.44 nm after coating with the Fe-EGCG layer (Fig. 1**C**). In addition, the surface potentials of $mSiO_2$, SC, and SC@FEG were –25.37 $\pm$ 0.66 mV, –26.85 $\pm$ 1.13 mV, and –32.38 $\pm$ 0.55 mV, respectively (Fig. 1**D**). TEM clearly demonstrated the typical porous structure of $mSiO_2$, whereas this porous structure disappeared in SC@FEG upon CXB loading and FEG coating (Fig. 1**E**), which was attributed to the pore filling by the drug and surface coverage via the coating, thereby indirectly confirming the successful fabrication of SC@FEG. Moreover, UV-Vis spectroscopy showed that SC@FEG exhibited the characteristic peak of CXB, alongside a red shift of the characteristic peak caused by the coordination interaction between EGCG and Fe^{3+} (Fig. 1**F**), offering spectroscopic evidence for the successful loading of CXB and formation of the FEG coating. Furthermore, FTIR spectra provided additional evidence supporting the successful synthesis of SC@FEG (Fig. 1G). In SC@FEG, the -OH stretching band of EGCG red-shifted from 3340 cm^{-1} to 3466 cm^{-1} due to Fe^{3+}-EGCG coordination, and the markedly weakened characteristic peaks

of CXB indicated its effective encapsulation within the mesoporous $mSiO_2$ mesopores, collectively corroborating the successful fabrication of the SC@FEG nanoplatform. Meanwhile, the EE% and LC% of CXB were determined to be (96.79 ± 0.71) % and (10.37 ± 0.08) %, respectively. Stability experiments demonstrated that the particle size of SC@FEG exhibited no significant fluctuation over 14 days in ultrapure water and DMEM medium (Fig. 1**H**), underscoring its satisfactory preliminary stability under both storage and physiological conditions.

Additionally, *in vitro* drug release studies investigated the cumulative release of CXB from SC@FEG under gradient H_2O_2 concentrations (0, 0.05, 0.1, 0.5, and 1 mM) (Fig. 1**I**). In the absence of H_2O_2, the cumulative release rates of SC@FEG were only 35.63 ± 5.76% at 12 hours and 46.67 ± 2.66% at 24 hours. Notably, even at a low H_2O_2 concentration of 0.05 mM, the cumulative release was significantly enhanced. This trend became more pronounced with increasing H_2O_2 concentration, with the release profile exhibiting a distinct H_2O_2 concentration-dependent acceleration. The cumulative release rates of SC@FEG markedly increased to 64.69 ± 5.19% at 12 hours and 86.93 ± 3.21% at 24 hours under 1 mM H_2O_2 (Fig. 1**I**). Thus, the synthesized SC@FEG nanoparticles possess an appropriate particle size, good stability, and robust ROS-responsive release properties, demonstrating their application potential as a promising drug delivery system for EMs treatment.

Evaluation of the Photothermal Performance of SC@FEG

Favorable photothermal conversion performance is a critical prerequisite for evaluating whether a material can be applied in PTT. Under the condition of a fixed laser power of 1.5 W/cm^2, the photothermal effect of SC@FEG showed a distinct concentration dependence (Fig. 2**A**). As the concentration of SC@FEG increased from 0 μg/mL to 200 μg/mL, the magnitude of temperature rise of the solution over time increased significantly. Specifically, when the concentration of SC@FEG was 0 μg/mL, the system temperature remained basically at the initial level, indicating that laser energy was not effectively absorbed and converted. In contrast, when the concentration of SC@FEG reached 200 μg/mL, the solution temperature rose rapidly to approximately 60 °C, demonstrating a positive correlation between concentration and photothermal conversion efficiency. Notably, the system temperature could rise from approximately 30 °C to above 50 °C within 10 minutes under 150 μg/mL SC@FEG, which had reached the effective temperature required for PTT [21], suggesting that the 150 μg/mL concentration of SC@FEG has potential applicability in PTT. Considering that high concentrations might increase the risk of *in vivo* toxic side effects, this concentration was selected for subsequent studies. Moreover, the relationship between laser power and photothermal effect was further explored. As shown in Fig. 2**B**, higher laser power led to a significant increase in both the temperature rise rate and the final temperature achieved by the solution, confirming an obvious positive correlation between laser intensity and SC@FEG-mediated photothermal conversion. Under a laser power of 1.5 W/cm^2, the solution temperature reached approximately 50 °C within 10 minutes, which was sufficient to meet the temperature requirement for PTT while avoiding potential tissue damage induced by excessive power. Therefore, the parameter combination of 150 μg/mL SC@FEG and 1.5 W/cm^2 laser power was adopted for the subsequent systematic evaluation of photothermal stability and photothermal imaging.

Photothermal cycle stability constitutes another vital indicator for measuring the application potential of photothermal materials. SC@FEG was subjected to five cycles of laser on/off irradiation, during which the solution temperature rapidly rose to approximately 55 °C upon irradiation and quickly returned to the initial temperature after the laser was turned off. Importantly, both heating and cooling curves remained nearly overlapping across all cycles, with almost no attenuation (Fig. 2**C**). In addition, the η of SC@FEG was calculated to be 30.14% (Fig. 2**D**). This relatively high η means that SC@FEG can convert more light energy into thermal energy under the same laser power and material concentration. Furthermore, temperature distribution images of SC@FEG and PBS were then captured at 0, 1, 2, 3, 4, 5, and 6 minutes under NIR irradiation (808 nm, 1.5 W/cm^2) to intuitively demonstrate the temporal dynamics of the photothermal effect (Fig. 2**E**). As shown in the images, the temperature of SC@FEG increased continuously throughout the irradiation period, thereby directly confirming the excellent photothermal conversion capacity of SC@FEG. Collectively, these properties underscore SC@FEG as a promising and reliable photothermal agent, providing strong support for its application in EMs therapy through PTT-based combination strategies.

In Vitro Assessment of the Therapeutic Efficacy of SC@FEG Combined With PTT Against EMs

Immunofluorescence staining and flow cytometry analyses were performed to verify the purity and identity of primary isolated eESCs. The immunofluorescence results showed that the isolated cells were positive for vimentin and negative for cytokeratin (Fig. 3**A**), which is consistent with the typical phenotype of endometrial stromal cells. Flow cytometry further quantified that the proportions of $CD45^-CD90^+$ and $CD45^-CD105^+$ cells were 96.68 ± 0.25% and 96.89 ± 0.94%, respectively (Fig. 3B), indicating that the purity of stromal cells exceeded 96%. These findings collectively confirm that the obtained eESCs exhibited high purity and homogeneity, thus meeting the requirements for subsequent functional experiments. To determine an appropriate concentration, the effect of CXB on eESCs viability was first examined using the CCK-8 assay across different concentration gradients (Fig. 3**C**). The results showed that the viability of eESCs decreased

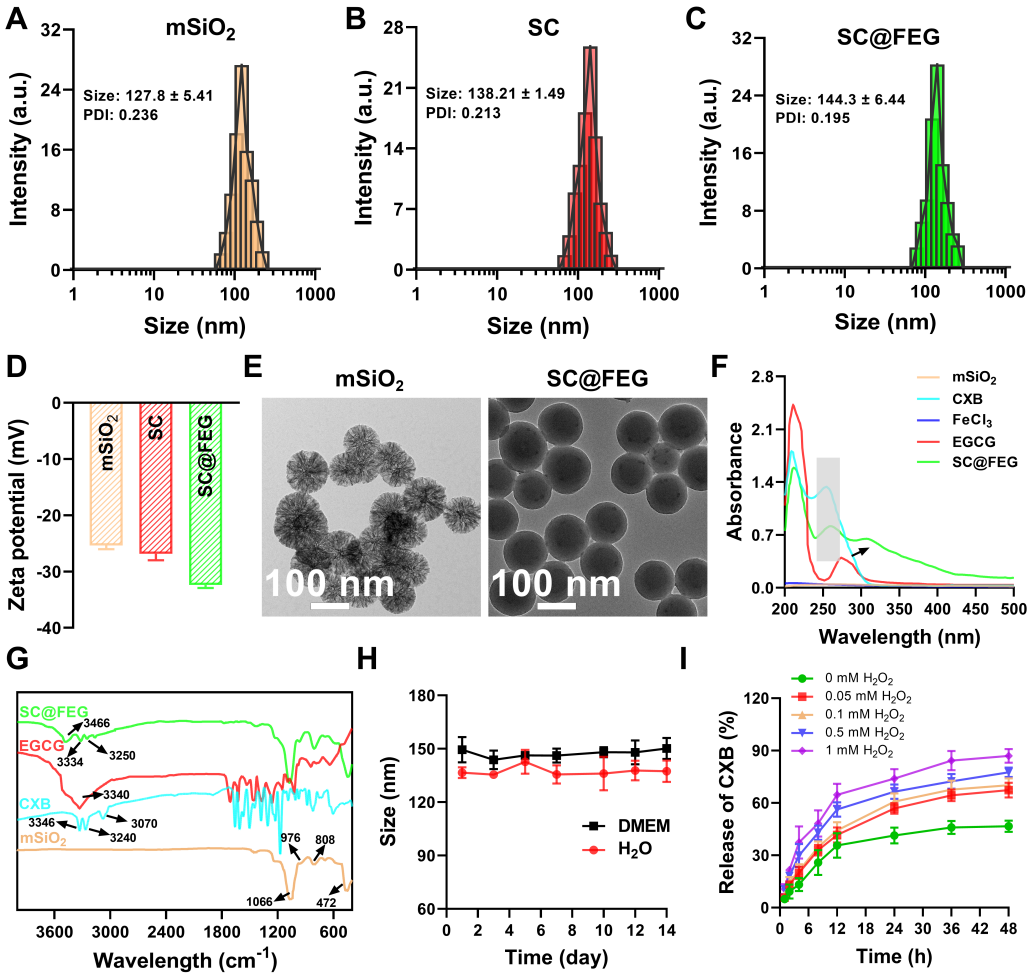

Fig. 1. Characterization of the physicochemical properties and ROS-responsive release behavior of SC@FEG. (**A–C**) Particle size distributions of $mSiO_2$, SC, and SC@FEG; (**D**) Zeta potentials of $mSiO_2$, SC, and SC@FEG; (**E**) TEM images of $mSiO_2$ and SC@FEG (scale bar: 100 nm); (**F**) UV-Vis absorption spectra; (**G**) FTIR spectra; (**H**) Stability curves of SC@FEG in DMEM medium and ultrapure water over 14 days; (**I**) Drug release profiles of CXB under different H_2O_2 concentrations (0, 0.05, 0.1, 0.5, and 1 mM). The images were plotted using GraphPad Prism 9.0 and WPS Office software.

in a concentration-dependent manner with increasing CXB concentration. When the concentration reached 40 μM, the cell viability was reduced to (64.56 $\pm$ 7.77) %. At this concentration, CXB could exert anti-inflammatory effects while avoiding the risk of non-specific toxicity, and also provide an observable space for the combined effect of SC@FEG and PTT. Accordingly, 40 μM was selected as the CXB administration concentration for subsequent *in vitro* experiments. Next, the viability of eESCs under different treatments with or without laser irradiation was compared (Fig. 3**D**). The results showed that the inhibitory effects of the Control and CXB groups on eESCs were unaffected by laser irradiation. In contrast, both S@FEG and SC@FEG exhibited significantly reduced cell survival following NIR irradiation (808 nm, 1.5 W/cm^2, 5 min) compared with non-irradiated conditions ($p < 0.01$, $p < 0.001$), which was mainly attributed to the photothermal conversion effect of the FEG coating. To more intuitively verify this result, Calcein-AM/PI double staining was further performed to observe the cell survival status (Fig. 3**E–F**). The results showed that the proportion of live cells in both S@FEG and SC@FEG groups was significantly reduced after NIR irradiation ($p < 0.01$, $p < 0.001$), which was consistent with the CCK-8 results, confirming that SC@FEG exerted cytotoxicity through a combined photothermal and drug killing effect.

Beyond direct cytotoxicity, the aberrant migration and invasion of eESCs also constitute pivotal processes in EMs progression and adhesion formation [22]. As depicted in Fig. 4**A–C**, the results of Transwell assays showed that cells in the Control group displayed vigorous migration and invasion, characterized by high cell counts and dense distribution. Both free CXB and S@FEG could significantly inhibit these processes ($p < 0.05$, $p < 0.01$, $p < 0.001$), which was mainly due to the inherent ability of CXB [23] and EGCG [24] to inhibit cell migration and invasion. SC@FEG treat-

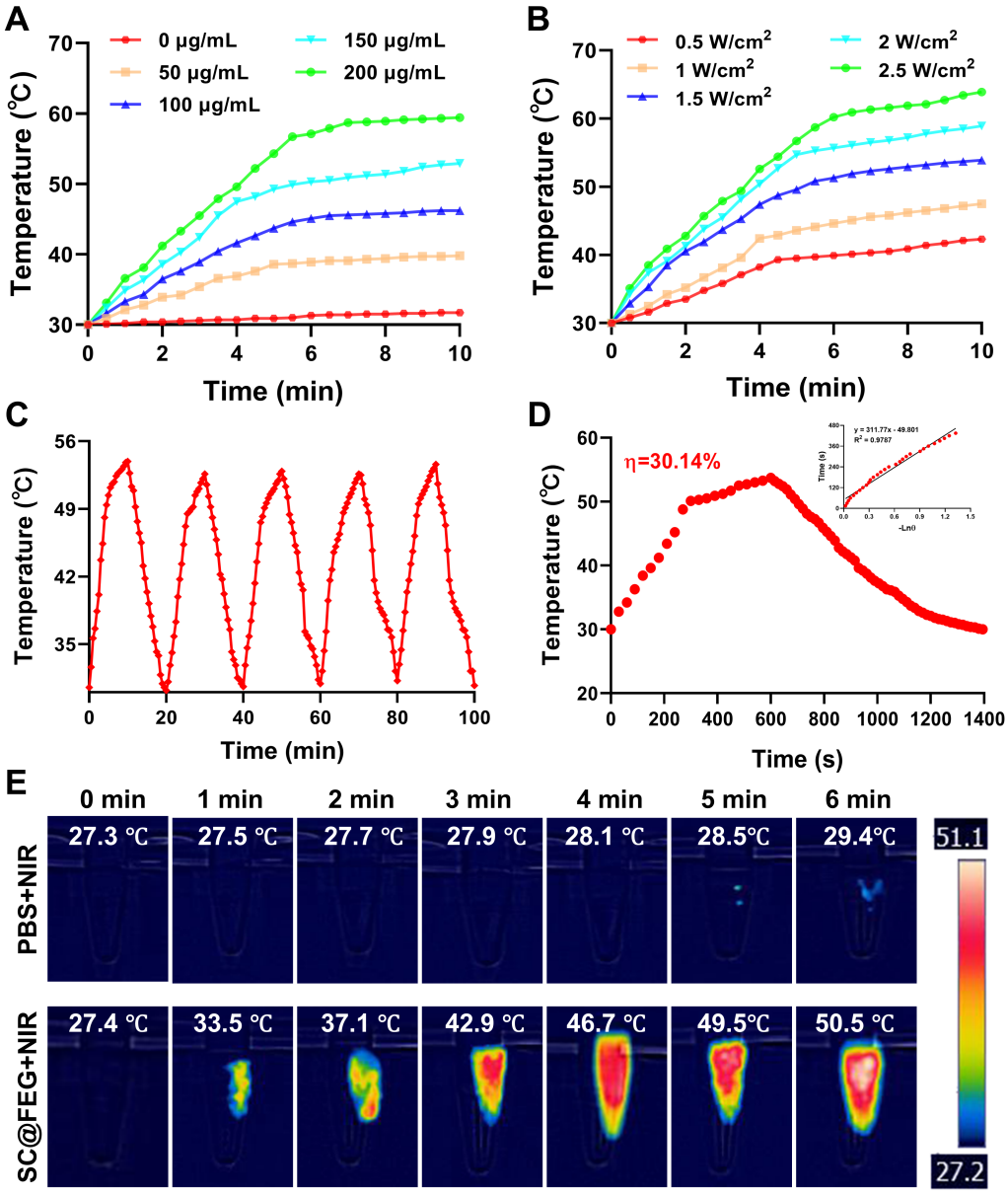

Fig. 2. The photothermal performance of SC@FEG. (**A**) Concentration-dependent temperature rise curves of SC@FEG under NIR; (**B**) Power density-dependent temperature rise curves of SC@FEG under NIR; (**C**) Photothermal conversion cycle stability and (**D**) η of SC@FEG; (**E**) Photothermal images of PBS and SC@FEG under NIR. The images were plotted using GraphPad Prism 9.0 and WPS Office software.

ment further amplified the inhibitory effects, which became most pronounced when combined with NIR irradiation ($p < 0.05$). These findings suggested that PTT contributed to direct structural damage of eESCs, thereby augmenting the suppression of migration and invasion, while the release of CXB concurrently suppressed malignant phenotypes via its anti-inflammatory effect.

As a key mediator of the inflammatory response in EMs, the high expression of COX2 can promote prostaglandin synthesis, exacerbate local inflammation, and drive cell proliferation, migration, and invasion [25]. Therefore, its protein expression level was detected by Western blot (Fig. 4**D**). As expected, CXB, a COX2 inhibitor, obviously downregulated the expression of COX2 ($p < 0.05$), while SC@FEG under NIR irradiation produced a substantially greater inhibitory effect ($p < 0.001$). This enhancement may be attributed to the increased cell membrane permeability induced by the photothermal effect, which in turn improved CXB bioavailability and strengthened COX2 inhibition. Consistent with the Western blot results, ELISA further revealed that SC@FEG combined with NIR irradiation significantly reduced the secretion of PGE_2 and pro-inflammatory cytokines (TNF-α, IL-1β, and IL-6) compared with all other groups ($p < 0.001$; Fig. 4**E**–

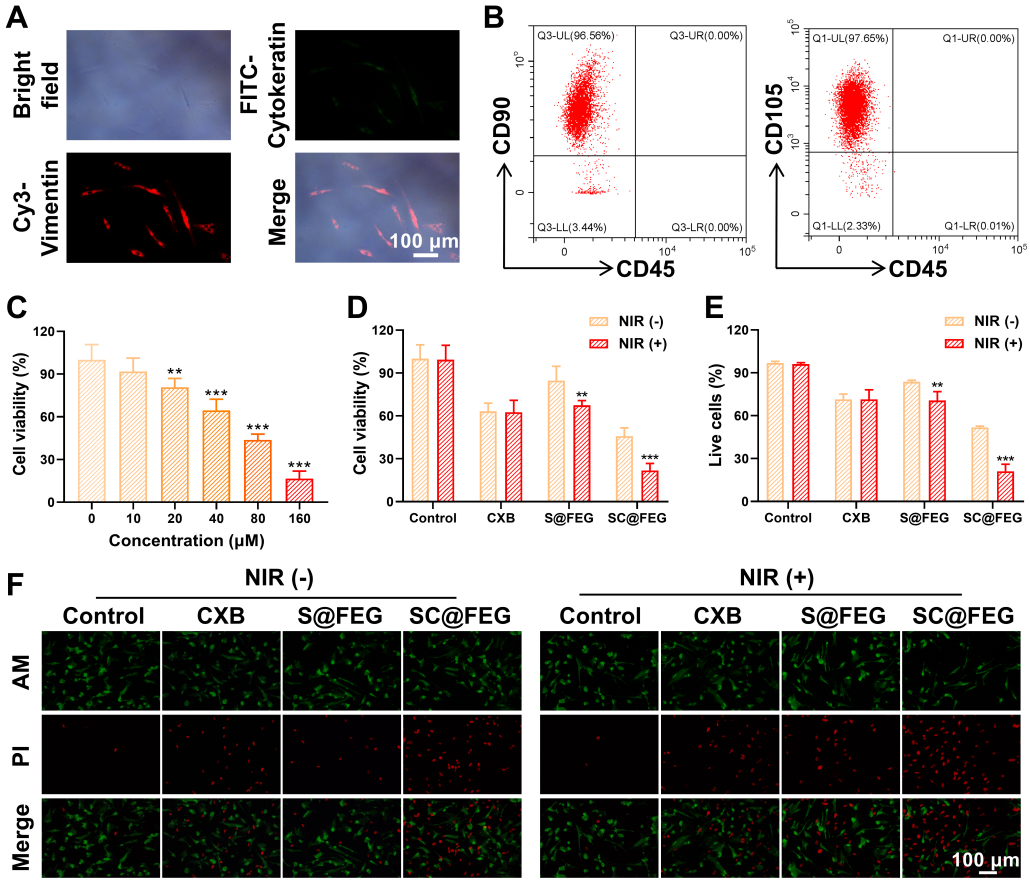

Fig. 3. Identification of primary eESCs and *in vitro* cytotoxicity of SC@FEG combined with PTT on eESCs. (**A**) Immunofluorescence staining of vimentin (red) and cytokeratin (green) in isolated eESCs (scale bar: 100 μm); (**B**) Flow cytometric analysis of $CD45^{-}CD90^{+}$ and $CD45^{-}CD105^{+}$ expression for eESC purity validation; (**C**) CXB concentration-dependent reduction in cell viability detected by CCK-8 assay; (**D**) Cell survival status of different treatment groups detected by CCK-8 assay, and (**E–F**) Calcein-AM/PI live/dead staining (scale bar: 100 μm). $^{**}p < 0.01$, $^{***}p < 0.001$, vs. 0 μM CXB or NIR (-) group. The images were plotted using GraphPad Prism 9.0 and WPS Office software.

F), directly confirming its potent anti-inflammatory activity at the cellular level. Together, these findings indicate that SC@FEG accentuates the overall anti-inflammatory response.

Combined with the above results, SC@FEG combined with NIR irradiation demonstrated superior efficacy over SC@FEG alone in suppressing eESCs viability, migration, invasion, and inflammatory signaling ($p < 0.05$, $p < 0.001$), which verified the comprehensive advantages of SC@FEG combined with PTT in the *in vitro* treatment of EMs from multiple perspectives.

The Curative Potential of SC@FEG Combined With PTT in the EMs Mouse Model

To further delineate the therapeutic potential of SC@FEG *in vivo*, a murine EMs model was established. Laparotomy performed 21 days after modeling revealed obvious ectopic lesions formed on the abdominal wall (Fig. 5**A**), and H&E staining showed typical endometrial glandular and stromal structures in the ectopic lesions (Fig. 5**B**), indicating the successful establishment of the *in vivo* EMs model. To further evaluate the *in vivo* biodistribution and determine the optimal timing for photothermal treatment, *in vivo* fluorescence imaging was performed using IR780-labeled nanoparticles (SI@FEG). As shown in Fig. 5**C**, SI@FEG exhibited progressive accumulation at the ectopic lesions, reaching the maximum signal intensity at 6 h post-injection. In contrast, free IR780 was predominantly distributed in the liver with no obvious enrichment in the lesions. These results indicate that the nanoplatform achieves effective lesion-targeted delivery, and 6 h post-injection was therefore selected as the optimal time point for NIR irradiation in subsequent photothermal therapy experiments. Accordingly, laser irradiation (808 nm, 1.5 W/cm^2) was applied to the lesion sites 6 hours after tail vein injection of SC@FEG. As demonstrated by thermal imaging (Fig. 5**D**), no obvious temperature elevation was observed in the PBS+NIR group, whereas the lesion temperature in the SC@FEG+NIR group exhibited a steady increase, reaching 48.7 °C at 3 minutes and 50.3 °C at 5 min. These findings

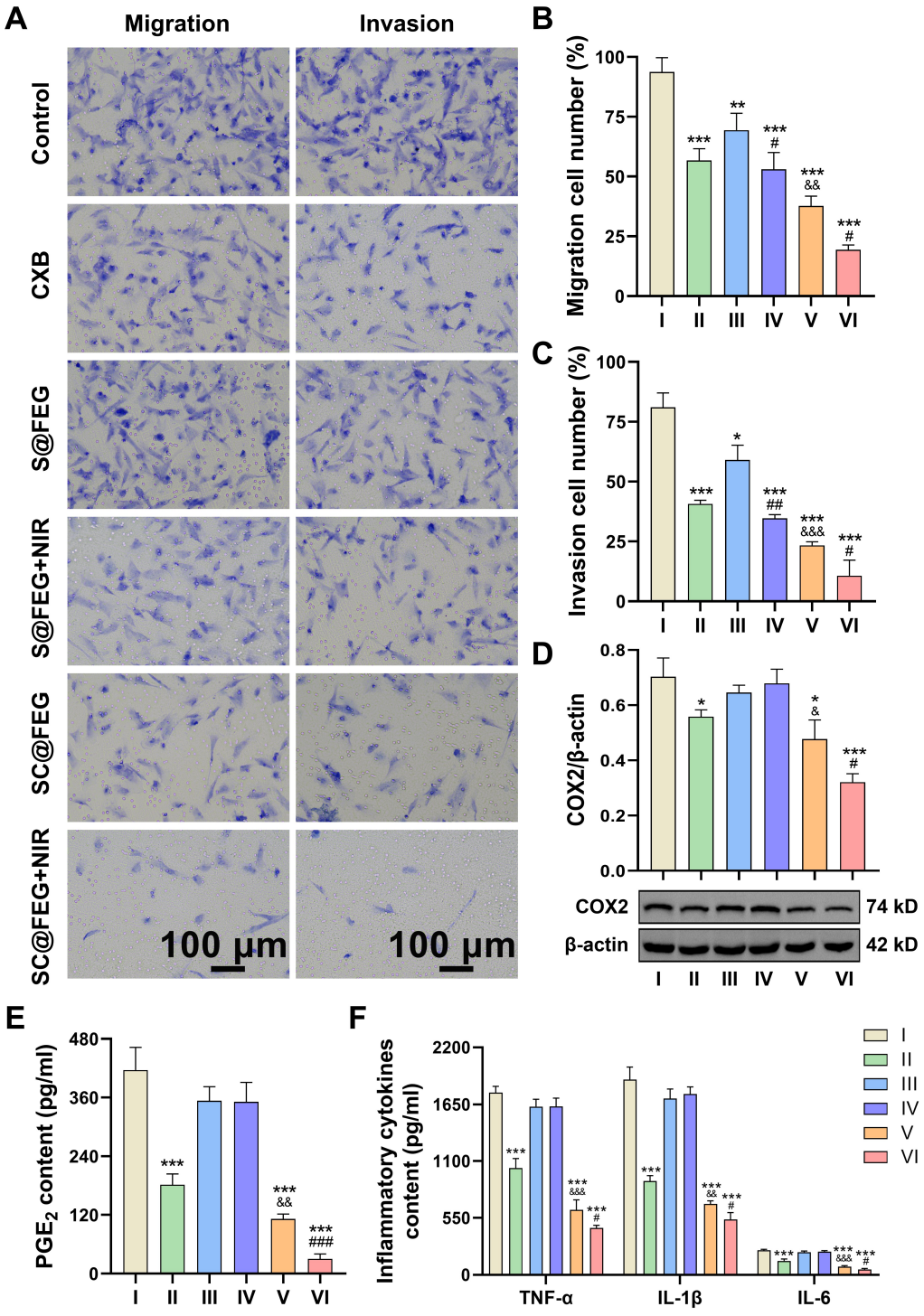

Fig. 4. Effects of SC@FEG combined with PTT on migration, invasion, and inflammation regulation of eESCs. (**A**) Representative images of migration (left) and invasion (right) assays (scale bar: 100 μm); (**B**) Quantified migration and (**C**) invasion cell number; (**D**) Western blot analysis of COX2 protein expression in eESCs with corresponding quantification. (**E–F**) ELISA results of PGE_2 and pro-inflammatory cytokines (TNF-α, IL-1β, IL-6). I: Control, II: CXB, III: S@FEG, IV: S@FEG+NIR, V: SC@FEG, VI: SC@FEG+NIR. $^{*}p < 0.05$, $^{**}p < 0.01$, $^{***}p < 0.001$, vs. Control group; $^{\#}p < 0.05$, $^{\#\#}p < 0.01$, $^{\#\#\#}p < 0.001$, vs. NIR (-) group; $^{\&}p < 0.05$, $^{\&\&}p < 0.01$, $^{\&\&\&}p < 0.001$ vs. CXB group. The images were plotted using GraphPad Prism 9.0 and WPS Office software.

indicated that SC@FEG effectively accumulated at the ectopic lesion site and achieved efficient photothermal conversion under NIR irradiation, thereby providing crucial energy for subsequent thermal ablation of ectopic lesions, in agreement with its photothermal properties observed *in vitro*.

In addition, the gross morphology and volume of ectopic lesions across different treatment groups intuitively reflected the therapeutic divergence among various intervention strategies (Fig. 5**E–F**). Lesions in the PBS group appeared dark red to blackish red with pronounced hemorrhage, suggestive of severe congestion and active inflammation at a progressive stage. CXB intervention resulted in reduced lesion volume ($p < 0.001$), lighter coloration, and alleviated hemorrhage, implying that CXB inhibited lesion progression to a certain extent by suppressing the inflammatory response. Likewise, treatment with S@FEG led to a certain degree of lesion volume reduction ($p < 0.001$) and inflammation attenuation, which might be related to the inherent anti-inflammatory and anti-invasion properties of EGCG [26]. Due to the ablative effect of PTT, S@FEG+NIR treatment could further reduce the lesion volume ($p < 0.001$) and lighten the appearance color. Notably, the SC@FEG+NIR group exhibited the most pronounced therapeutic outcome, as lesions were minimized in size and presented a pale pink to nearly translucent appearance with almost no obvious blood supply or bleeding. This suggested that ROS-responsive CXB release combined with photothermal ablation could more efficiently suppress the inflammatory response and eliminate ectopic lesions. To ensure systemic tolerance, body weight was monitored during treatment (Fig. 5**G**). Mice in all groups displayed steady weight gain with no significant intergroup differences, thereby preliminarily excluding the adverse effects of PTT and SC@FEG at the applied dosage.

TUNEL and Masson staining were further performed to observe the apoptosis and fibrosis degree of ectopic lesions (Fig. 5**H–J**). The results showed that almost no apoptotic cells were observed in the lesions of the PBS group, while a large number of TUNEL-positive cells were observed after SC@FEG+NIR treatment ($p < 0.001$). In parallel, Masson staining revealed extensive blue-stained areas in the PBS group, reflecting obvious collagen deposition and fibrosis. Strikingly, lesions in the SC@FEG+NIR group exhibited a substantial reduction in collagen accumulation ($p < 0.001$).

Modulatory Effect of SC@FEG Combined with PTT on Inflammation in EMs in Vivo

EMs is characterized by estrogen-dependent inflammatory responses, targeted inhibition of COX2 expression and related inflammatory factors represents a critical strategy for alleviating EMs inflammation and curbing lesion progression (Fig. 6**A**). Based on this, the anti-inflammatory potential of SC@FEG combined with PTT was further examined *in vivo* at the molecular level. Western blot analysis revealed that SC@FEG+NIR treatment exerted the most pronounced suppression of COX2 protein expression in ectopic lesions (Fig. 6**B**). This robust inhibitory effect was likely attributable to the targeted delivery capability of SC@FEG, which enabled the accumulation of CXB at lesion sites, while the NIR-induced photothermal effect enhanced cell membrane permeability. These features enhanced the bioavailability of CXB in local lesions, allowing for potent inhibition of COX2 and thereby mitigating lesion-associated inflammation. To further substantiate the anti-inflammatory mechanism of CXB-mediated COX2 inhibition, the PGE_2 levels in ectopic lesion tissues were measured via ELISA. The results showed that SC@FEG+NIR treatment led to the most significant reduction in lesion PGE_2 levels ($p < 0.001$), which was more pronounced than SC@FEG alone ($p < 0.001$), confirming that the nanoplatform effectively blocks COX2-mediated PGE_2 synthesis in EMs lesions (Fig. 6**C**). In addition, the systemic cytokine levels corroborated these findings (Fig. 6**D**). Treatment with CXB, SC@FEG, and SC@FEG+NIR all remarkably reduced the TNF-α, IL-6, and IL-1β levels ($p < 0.05$, $p < 0.01$, $p < 0.001$). Notably, SC@FEG achieved superior anti-inflammatory effects compared with free CXB ($p < 0.01$), while the addition of NIR irradiation did not produce a further significant improvement relative to SC@FEG alone.

Biosafety Evaluation of SC@FEG Combined With PTT

Biosafety constitutes a core prerequisite for the clinical translation of nanomedicines, so the hemocompatibility, histocompatibility, and systemic toxicity of SC@FEG combined with PTT were systematically evaluated. Hemolysis assays demonstrated that under NIR irradiation, the hemolysis rate of SC@FEG across all tested concentrations remained below 3% (Fig. 7**A–B**), which was lower than the safety threshold of 5% [20]. This indicated that the nanosystem had good hemocompatibility in the blood circulation without inducing hemolytic adverse effects, thereby providing a safe basis for intravenous delivery. Moreover, after treatment, major organs, including the ovary, uterus, heart, liver, spleen, lung, and kidney, were harvested for H&E staining to examine the potential histological toxicity (Fig. 7**C**). The results showed that no obvious tissue damage or pathological abnormalities were observed, such as inflammatory infiltration, necrosis, or tissue structure disorder. These findings demonstrated that SC@FEG combined with PTT had good histocompatibility, and SC@FEG could selectively exert its therapeutic effect on endometriotic lesions without causing significant damage to normal tissues. Furthermore, hematological and biochemical assessments provided additional validation. All parameters, encompassing RBC, WBC, PLT, HGB, ALT, AST, CK, and LDH, remained in normal physiological ranges, with no significant differences between the SC@FEG+NIR and PBS groups (Fig. 7**D**). Collectively, these findings confirmed that SC@FEG combined with PTT exhibited an excellent biosafety profile, neither perturbing hematological indices nor impairing hepatic or cardiac function, thereby eliminating concerns of systemic toxicity.

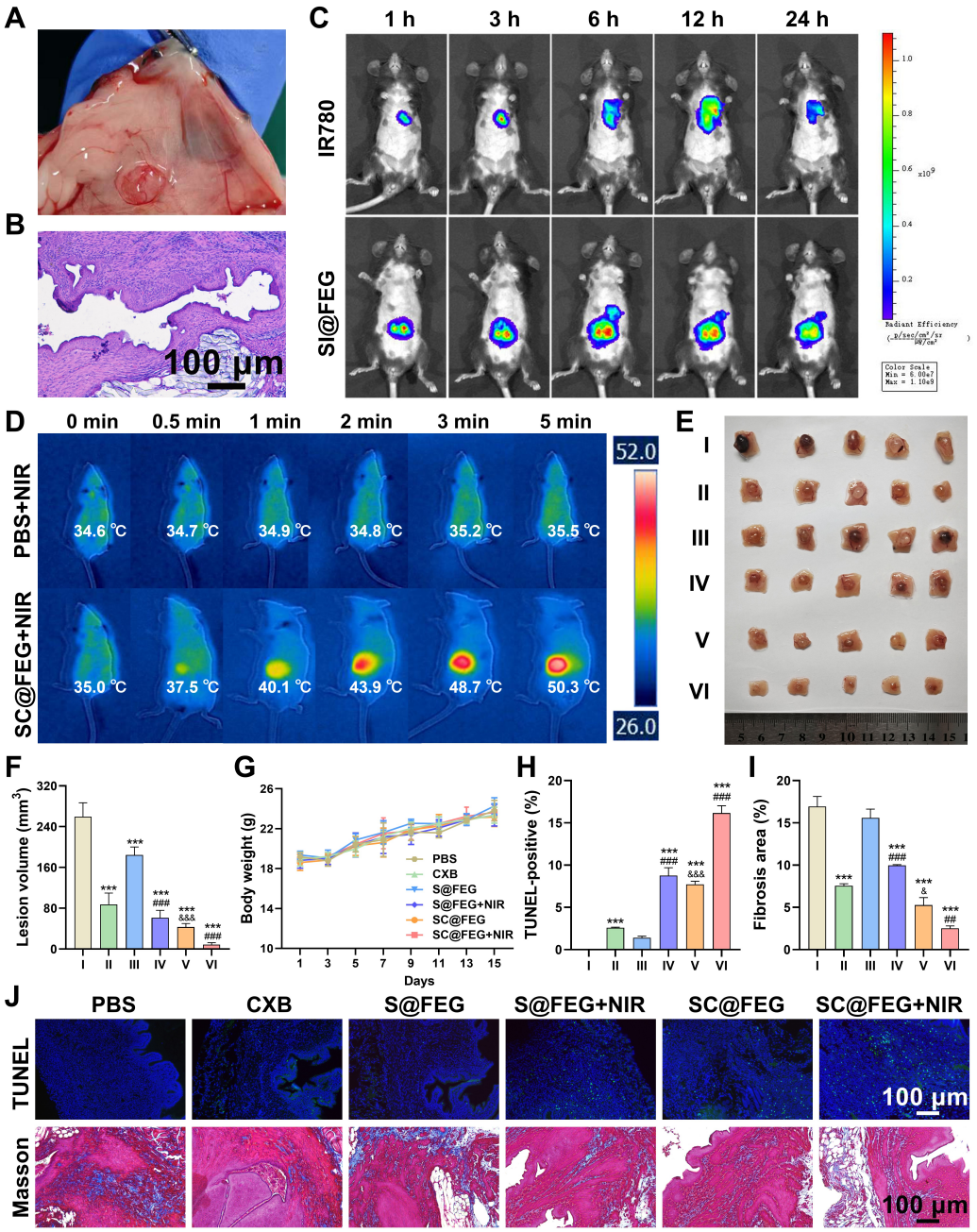

Fig. 5. ***In vivo*** **therapeutic evaluation of SC@FEG combined with PTT against EMs.** (**A**) Gross observation of ectopic lesions on the abdominal wall of mice 21 days after modeling; (**B**) H&E staining results of ectopic tissues (scale bar: 100 μm); (**C**) *In vivo* fluorescence imaging of SI@FEG and free IR780 at indicated time points post-injection; (**D**) Photothermal images of PBS and SC@FEG under NIR irradiation (808 nm, 1.5 W/cm^2); (**E**) Gross morphology and (**F**) volume of ectopic lesions from mice subjected to different treatments; (**G**) Body weight change curves of mice in each group during treatment; (**H–J**) TUNEL and Masson's trichrome staining of ectopic lesions with quantitative results (scale bar: 100 μm). I: Control, II: CXB, III: S@FEG, IV: S@FEG+NIR, V: SC@FEG, VI: SC@FEG+NIR. ***$p < 0.001$ vs. PBS group; $^{\#\#}p < 0.01$, $^{\#\#\#}p < 0.001$ vs. NIR (-) group; $^{\&}p < 0.05$, $^{\&\&\&}p < 0.001$ vs. CXB group. The images were plotted using GraphPad Prism 9.0 and WPS Office software.

Discussion

Endometriosis is a chronic estrogen-dependent inflammatory disease characterized by ectopic implantation of endometrial tissue, persistent inflammation, oxidative stress, fibrosis, and high recurrence rates [27]. In this study, we successfully constructed SC@FEG, which integrates both photothermal effects and ROS-responsive drug delivery capabilities, and systematically verified its multiple advantages in treating EMs when combined with PTT. SC@FEG exhibited efficient NIR-induced photothermal conversion, which induced eESCs' death and sup-

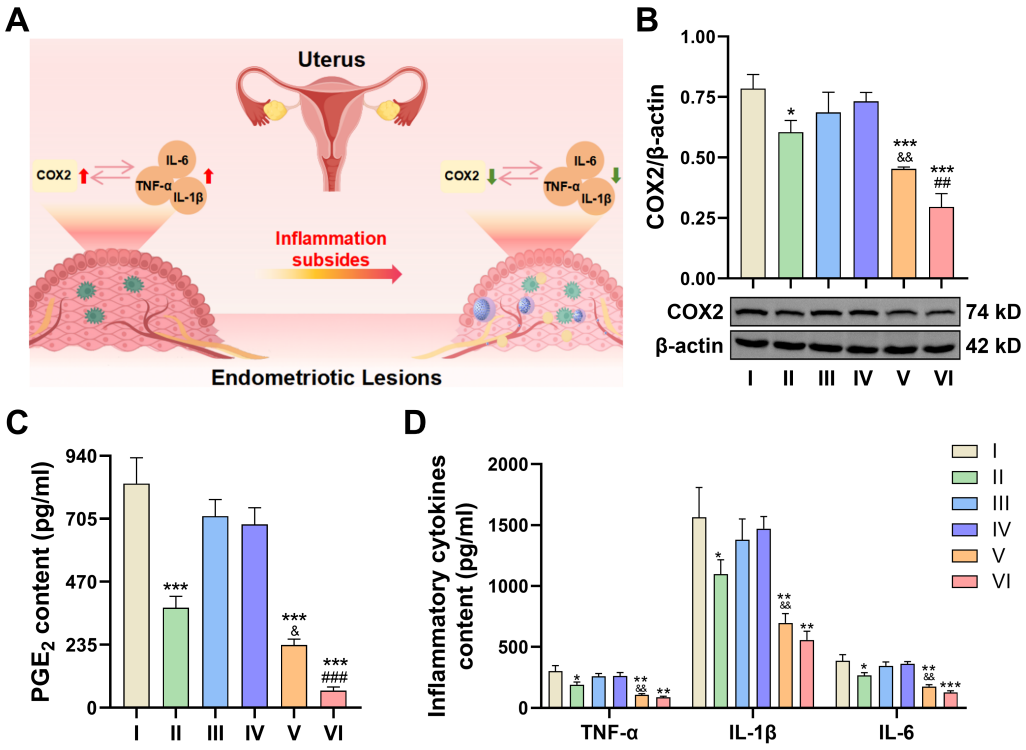

Fig. 6. Assessment of the anti-inflammatory modulation of SC@FEG combined with PTT *in vivo*. (**A**) Dynamic changes of the inflammatory cascade in EMs; (**B**) Detection and quantitative analysis of COX2 protein expression in ectopic lesion tissues by Western blot; (**C–D**) Levels of PGE_2, TNF-α, IL-6, and IL-1β in mouse serum detected by ELISA. I: Control, II: CXB, III: S@FEG, IV: S@FEG+NIR, V: SC@FEG, VI: SC@FEG+NIR. *$p < 0.05$, **$p < 0.01$, ***$p < 0.001$, vs. PBS group; $^{\#\#}p < 0.01$, $^{\#\#\#}p < 0.001$, vs. NIR (-) group; $^{\&}p < 0.05$, $^{\&\&}p < 0.01$, vs. CXB group. The images were plotted using GraphPad Prism 9.0 and WPS Office software.

pressed their migration and invasion, while ROS-triggered CXB release further enhanced the anti-inflammatory efficacy *in vitro*. Moreover, *in vivo* experiments demonstrated that SC@FEG selectively accumulated in ectopic lesions, where combined photothermal ablation and targeted CXB delivery synergistically inhibited lesion growth, promoted apoptosis, alleviated fibrosis, reduced systemic inflammation, and ultimately achieved efficient suppression of EMs progression. More importantly, this nanosystem possesses excellent hemocompatibility and histocompatibility, with no detectable damage to major organs or hematological abnormalities, ensuring its translational potential.

The rational design of SC@FEG addresses several key limitations of conventional EMs therapy. The successful construction of SC@FEG was supported by multiple physicochemical characterization results. The gradual increase in particle size following CXB loading and Fe-EGCG coating is consistent with the typical enlargement behavior of nanocarriers after drug encapsulation and surface functionalization. The Fe^{3+}-EGCG coordination structure was further supported by the spectroscopic evidence, which is highly consistent with previously reported metal-polyphenol coordination systems [28]. Moreover, the relatively negative surface potential of SC@FEG may contribute to facilitating the maintenance of good dispersive stability in aqueous solutions. In addition, the excellent stability of SC@FEG under both storage and physiological conditions may be beneficial for ensuring reproducibility and controllability of nanomedicines in prospective clinical applications. Notably, one of the most significant advantages of SC@FEG is its ROS-responsive drug release behavior. Given that ectopic lesion tissues generally exhibit the pathological feature of elevated ROS levels [29], such a concentration-dependent ROS-responsiveness is of great value for EMs treatment. It enables SC@FEG to remain stable during systemic circulation and avoids systemic side effects caused by premature drug release, while facilitating rapid CXB release triggered by the high-ROS microenvironment at pathological sites, thereby ensuring precise and efficient CXB delivery to lesions. Compared with conventional non-responsive nanoplatforms, this environment-triggered drug release mode offered superior therapeutic selectivity and safety [30].

Another important finding of this study is that SC@FEG combined with PTT significantly enhanced the therapeutic efficacy against eESCs. The core mechanism of the PTT lies in the absorption of NIR light by nanomaterials, which is subsequently converted into thermal energy capable of inducing cell death through cell membrane structure disruption, protein denaturation, and other pathways

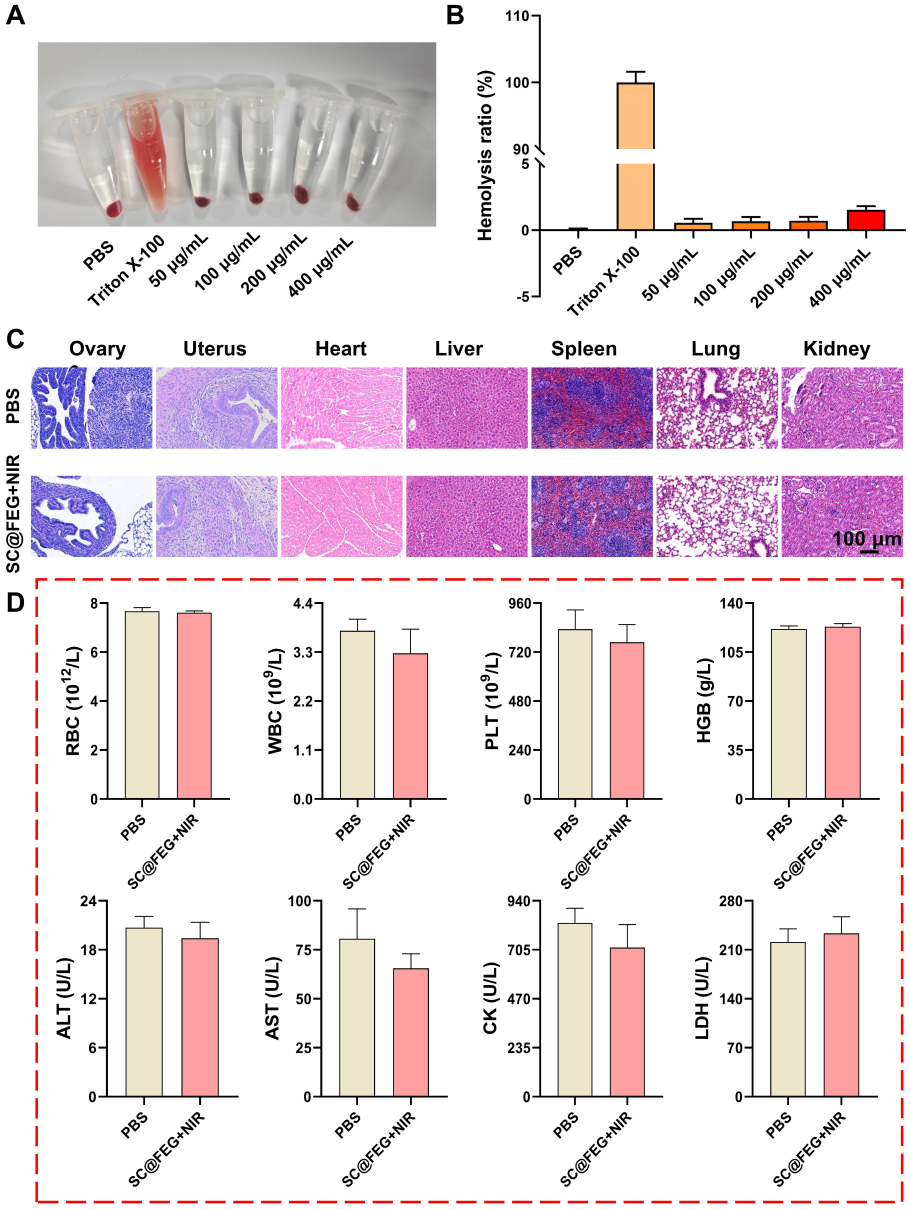

Fig. 7. Biosafety evaluation of SC@FEG combined with PTT. (**A–B**) Observation and quantitative comparison of hemolysis induced by SC@FEG at different concentrations under NIR irradiation; (**C**) H&E staining of ovarian, uterine, cardiac, hepatic, splenic, pulmonary, and renal tissues to assess histopathological alterations (scale bar: 100 μm); (**D**) Hematological and serum biochemical analyses. The images were plotted using GraphPad Prism 9.0 and WPS Office software.

[31]. Although PTT has been extensively explored in oncology, its application in EMs remains relatively limited. Owing to the superficial distribution and invasive growth characteristics of ectopic lesions, localized hyperthermia represents a rational strategy for selective lesion ablation while minimizing injury to surrounding tissues [15]. Moreover, SC@FEG possessed excellent photothermal stability, which could maintain stable photothermal conversion ability under multiple photothermal stimulations and thereby reduce the risk of performance degradation during treatment. From the perspective of clinical practical application, for PTT that requires multiple irradiations or continuous treatment, this material can function repeatedly without reducing the therapeutic effect, avoiding the cumbersomeness and potential risks of frequent material replacement. Our *in vitro* findings demonstrated that SC@FEG exhibited efficient and stable photothermal conversion under NIR irradiation, and the addition of PTT substantially enhanced the suppression of eESC viability, migration, and invasion compared with anti-inflammatory treatment alone. These results suggest that photothermal ablation may compensate for the limitations of conventional pharmacological therapy, which often suppresses inflammation but fails to directly eliminate ectopic lesions.

Chronic inflammation driven by the COX2/PGE_2 axis is recognized as a central mechanism underlying EMs progression, pain sensitization, and lesion persistence [32]. Meanwhile, the excessive secretion of pro-inflammatory cytokines such as TNF-α, IL-1β, and IL-6 further exacerbates the inflammatory level of EMs lesions, closely correlating with disease severity and clinical symptoms [33]. In the present study, SC@FEG effectively reduced COX2 expression and decreased the levels of PGE2 and pro-inflammatory cytokines both *in vitro* and *in vivo*, indicating enhanced anti-inflammatory efficacy after nanoformulation. Interestingly, while NIR irradiation further improved lesion ablation and apoptosis induction, its contribution to systemic cytokine suppression appeared relatively limited. This suggested that the anti-inflammatory efficacy was primarily derived from the lesion-targeting enrichment of SC@FEG, whereas the photothermal effect primarily functioned by promoting local cell apoptosis and lesion ablation, rather than direct cytokine suppression. The observed reductions in TNF-α, IL-6, and IL-1β hold important clinical implications for EMs management, as these pro-inflammatory cytokines are key mediators of EMs-associated pain and disease progression, all of which contribute to the chronic pelvic pain and dysmenorrhea that severely impact quality of life in EMs patients [34]. By lowering systemic levels of these cytokines, SC@FEG not only suppresses the inflammatory cascade at the lesion site but also alleviates the neuroinflammatory and nociceptive processes underlying EMs-related pain. This link between cytokine downregulation and pain relief underscores the translational relevance of SC@FEG as a dual-functional nanoplatform, as it addresses both the pathological growth of ectopic lesions and the debilitating clinical symptoms of EMs, a critical unmet need in current EMs therapy. It is noteworthy that although PTT may trigger cell necrosis and DAMP release to elicit mild local inflammation, targeted CXB delivery efficiently inhibits the COX-2/PGE_2 cascade and suppresses downstream pro-inflammatory cytokines. Meanwhile, EGCG scavenges excess ROS and relieves oxidative stress caused by Feion metabolism and Fenton reactions. Such synergistic anti-inflammatory and antioxidant effects effectively counteract the potential pro-inflammatory side effects of photothermal treatment, ensuring the overall therapeutic advantage of SC@FEG+NIR against endometriotic lesions.

In addition to inflammation suppression, apoptosis activation and fibrosis attenuation represent the clinically meaningful findings of this study. The occurrence and development of EMs are frequently accompanied by apoptosis resistance and abnormal fibrosis [35]. As a defining pathological feature of EMs, apoptosis resistance enables ectopic endometrial cells to survive and proliferate continuously in an adverse microenvironment, thereby fueling lesion development [36]. Meanwhile, fibrosis manifests as excessive deposition of collagen fibers within the lesion, not only disrupting local tissue architecture but also being closely associated with chronic pelvic pain and infertility [18]. Consequently, the capacity to effectively induce apoptosis while simultaneously mitigating fibrosis constitutes an important indicator in evaluating the efficacy of novel treatment strategies. Our results demonstrated that SC@FEG combined with PTT markedly induced cell apoptosis and alleviated collagen deposition within ectopic lesions. TUNEL staining suggests active proliferation and pronounced resistance to cell death, consistent with the pathological feature of apoptosis resistance in EMs, while SC@FEG combined with PTT effectively activated the programmed cell death pathway and significantly induced apoptosis of abnormally proliferative eESCs. It is worth noting that the alleviation of fibrosis of the combination therapy likely arises from the combined action of multiple components in this therapeutic system. On the one hand, the localized hyperthermia generated by PTT may directly ablate fibrotic tissues and facilitate collagen degradation [37]. On the other hand, CXB has been reported to suppress fibrosis by inhibiting both canonical and non-canonical TGF-β signaling pathways [38]. In addition, EGCG is known to exert anti-fibrotic effects by modulating key fibrotic pathways [39]. Together, these complementary mechanisms contribute to the observed reduction in lesion fibrosis. Therefore, the SC@FEG+NIR strategy not only eliminates ectopic lesions but also contributes to improving the pathological microenvironment of EMs lesions, which is clinically important for relieving patient pain and improving fertility.

Importantly, the current nanosystem demonstrated favorable biosafety without evident hematological abnormalities or major organ toxicity, supporting its translational potential. Nevertheless, several limitations should be acknowledged. First, the *in vivo* photothermal parameters (808 nm, 1.5 W/cm^2) were optimized based on a superficial abdominal wall EMs model, and a systematic evaluation of NIR light penetration and energy attenuation across varying tissue depths was not performed. Therefore, the applicability of the current irradiation settings to deeper or anatomically variable lesions requires further investigation. Moreover, long-term pharmacokinetics, biodegradation, and reproductive safety warrant additional investigation before clinical application.

Conclusions

In summary, this study proposes and validates the efficacy and safety of ROS-responsive nanoplatforms delivering COX2 inhibitors combined with PTT for the treatment of EMs. Our findings demonstrated that SC@FEG possesses stable physicochemical properties, efficient ROS-triggered drug release, and excellent photothermal conversion capability. Both *in vitro* and *in vivo* experiments confirmed that SC@FEG combined with NIR irradiation effectively suppressed eESC proliferation, migration, invasion, and inflammatory responses, while also promoting lesion

apoptosis, alleviating fibrosis, and reducing systemic inflammation, without evident toxicity. By uniting photothermal ablation with targeted anti-inflammatory intervention, SC@FEG offers a novel and precise therapeutic strategy, providing new insights for the clinical management of EMs.

Availability of Data and Materials

All data reported in this paper will also be shared by the corresponding author upon request.

Author Contributions

XZ contributed to the design of this work. YSZ and DHH contributed to the interpretation of data. YSZ and JWH analyzed the data. XZ drafted the work. DHH and JWH. revised critically for important intellectual content. All authors read and approved the final manuscript. All authors agree to be accountable for all aspects of the work in ensuring that questions related to the accuracy or integrity of any part of the work are appropriately investigated and resolved.

Ethics Approval and Consent to Participate

All experimental procedures were approved by the Experimental Animal Management and Ethics Committee of Wenzhou Medical University (Approval No. wydw-2025-0463).

Acknowledgments

Not applicable.

Funding

This research was funded by the Wenzhou Science and Technology Bureau Project, grant number Y20210558.

Conflict of Interest

The authors declare no conflict of interest.

References

[1] Kong H, Fan W, Ye T, Du L. Endometriosis does not impact aneuploidy rates of products of conception in IVF population. Scientific reports. 2025; 15: 2193. https://doi.org/10.1038/s41598-025-86656-x.

[2] Zondervan KT, Becker CM, Missmer SA. Endometriosis. The New England journal of medicine. 2020; 382: 1244–1256. https://doi.org/10.1056/NEJMra1810764.

[3] Li Q, Yuan M, Jiao X, Huang Y, Li J, Li D, *et al*. M1 Macrophage-Derived Nanovesicles Repolarize M2 Macrophages for Inhibiting the Development of Endometriosis. Frontiers in immunology. 2021; 12: 707784. https://doi.org/10.3389/fimmu.2021.707784.

[4] Moses AS, Taratula OR, Lee H, Luo F, Grenz T, Korzun T, *et al*. Nanoparticle-Based Platform for Activatable Fluorescence Imaging and Photothermal Ablation of Endometriosis. Small. 2020; 16: e1906936. https://doi.org/10.1002/smll.201906936.

[5] Rowlands IJ, Abbott JA, Montgomery GW, Hockey R, Rogers P, Mishra GD. Prevalence and incidence of endometriosis in Australian women: a data linkage cohort study. BJOG: an international journal of obstetrics and gynaecology. 2021; 128: 657–665. https://doi.org/10.1111/1471-0528.16447.

[6] Alotaibi FT. Pathophysiology of Endometriosis: Insights from Immunohistochemical Analysis of Ectopic and Eutopic Tissues. International journal of molecular sciences. 2025; 26: 5998. https://doi.org/10.3390/ijms26135998.

[7] Wang T, Ji M, Yang P, Zhang J, Peng X, Miao Y, *et al*. Cyclooxygenase 2 overexpression suppresses Smad3 and augments ERK1/2 signaling activated by TGFβ1 in endometrial stromal cells: A novel insight into endometriosis pathogenesis. Molecular and cellular endocrinology. 2025; 599: 112470. https://doi.org/10.1016/j.mce.2025.112470.

[8] Ding Y, Yang X, Wei Q, Bi X, Zhang Y, Ma Y, *et al*. Macranthoidin B restrains the epithelial-mesenchymal transition through COX-2/PGE(2) pathway in endometriosis. Frontiers in pharmacology. 2024; 15: 1492098. https://doi.org/10.3389/fphar.2024.1492098.

[9] Jeon D, Kim KT, Baek MJ, Kim DH, Lee JY, Kim DD. Preparation and evaluation of celecoxib-loaded proliposomes with high lipid content. European journal of pharmaceutics and biopharmaceutics : official journal of Arbeitsgemeinschaft für Pharmazeutische Verfahrenstechnik e.V. 2019; 141: 139–148. https://doi.org/10.1016/j.ejpb.2019.05.025.

[10] Sun Q, Lei Y, Zhang H, Ding X, Yang M, Zhang T, et al. A multifunctional nanoparticle for efferocytosis and pro-resolving-mediated endometriosis therapy. Colloids Surf B Biointerfaces. 2022; 220: 112893. https://doi.org/10.1016/j.colsurfb.2022.112893.

[11] Guimarães RS, Rodrigues CF, Moreira AF, Correia IJ. Overview of stimuli-responsive mesoporous organosilica nanocarriers for drug delivery. Pharmacological research. 2020; 155: 104742. https://doi.org/10.1016/j.phrs.2020.104742.

[12] Zhou P, Ma X, Hu Y, Chen Y, Wang H, Wang T, *et al*. Sericin-based dual-module microspheres promote periodontal regeneration through four-dimensional microenvironment remodeling. Biomaterials. 2026; 328: 123843. https://doi.org/10.1016/j.biomaterials.2025.123843.

[13] Wang C, Xiao R, Yang Q, Pan J, Cui P, Zhou S, *et al*. Green synthesis of epigallocatechin gallate-ferric complex nanoparticles for photothermal enhanced antibacterial and wound healing. Biomedicine & pharmacotherapy = Biomédecine & pharmacothérapie. 2024; 171: 116175. https://doi.org/10.1016/j.biopha.2024.116175.

[14] Liu MD, Guo DK, Zeng RY, Guo WH, Ding XL, Li CX, *et al*. Transformable Spinose Nanodrums with Self-Supplied H(2) O(2) for Photothermal and Cascade Catalytic Therapy of Tumor. Small Methods. 2021; 5: e2100361. https://doi.org/10.1002/smtd.202100361.

[15] Talukdar S, Singh SK, Mishra MK, Singh R. Emerging trends in nanotechnology for endometriosis: diagnosis to therapy. Nanomaterials (Basel, Switzerland). 2024; 14: 976. https://doi.org/10.3390/nano14110976.

[16] Tian W, Wang C, Chu R, Ge H, Sun X, Li M. Injectable hydrogel nanoarchitectonics with near-infrared controlled drug delivery for in situ photothermal/endocrine synergistic endometriosis therapy. Biomaterials Research. 2023; 27: 100. https://doi.org/10.1186/s40824-023-00442-2.

[17] Yuxue J, Ran S, Minghui F, Minjia S. Applications of nanomaterials in endometriosis treatment. Frontiers in bioengineering and biotechnology. 2023; 11: 1184155. https://doi.org/10.3389/fbioe.2023.1184155.

[18] Tang Z, Zhang X, Meng S, Yi X, Liu Y, Wu K, *et al*. Cell membrane camouflaged and ROS responsive nanosomes for targeted endometriosis therapy via reversing inflammatory, low-autophagy, and immunotolerant microenvironment. Chemical Engineering Journal. 2024; 493: 152697. https://doi.org/10.1016/j.cej.2024.152697.

[19] Ma J, Liao Z, Li J, Li X, Guo H, Zhong Q, *et al*. A cRGD-modified liposome for targeted delivery of artesunate to inhibit angiogenesis in endometriosis. Biomaterials science. 2025; 13: 1045–1058. https://doi.org/10.1039/d4bm01506a.

[20] Golafshan N, Rezahasani R, Tarkesh Esfahani M, Kharaziha M,

Khorasani SN. Nanohybrid hydrogels of laponite: PVA-Alginate as a potential wound healing material. Carbohydrate polymers. 2017; 176: 392–401. https://doi.org/10.1016/j.carbpol.2017.08.070.

[21] Mohamed M, Borchard G, Jordan O. In situ forming implants for local chemotherapy and hyperthermia of bone tumors. Journal of drug delivery science and technology. 2012; 22: 393–408. https://doi.org/10.1016/s1773-2247(12)50066-3.

[22] Wei N, Guan H, Zhang Y, Shi J, Ma J, Shi R, *et al*. Molecular mechanisms underlying the inhibition of cell migration and invasion in endometriosis: Advances in pharmacological research. Biomedical Reports. 2025; 23: 152. https://doi.org/10.3892/br.2025.2030.

[23] Xiong S, Huang W, Liu X, Chen Q, Ding Y, Huang H, *et al*. Celecoxib Synergistically Enhances MLN4924-Induced Cytotoxicity and EMT Inhibition Via AKT and ERK Pathways in Human Urothelial Carcinoma. Cell transplantation. 2022; 31: 9636897221077921. https://doi.org/10.1177/09636897221077921.

[24] Li F, Hao S, Gao J, Jiang P. EGCG alleviates obesity-exacerbated lung cancer progression by STAT1/SLC7A11 pathway and gut microbiota. The Journal of nutritional biochemistry. 2023; 120: 109416. https://doi.org/10.1016/j.jnutbio.2023.109416.

[25] Dan W, Yiling J, Chun L, Jing F, Huimin W, Xiaoxin Y. Withaferin A downregulates COX-2/NF-κB signaling and modulates MMP-2/9 in experimental endometriosis. Tropical Journal of Pharmaceutical Research. 2022; 20: 239–248. https://doi.org/10.4314/tjpr.v20i2.3.

[26] Kim S, Lee H, Moon H, Kim R, Kim M, Jeong S, *et al*. Epigallocatechin-3-Gallate Attenuates Myocardial Dysfunction via Inhibition of Endothelial-to-Mesenchymal Transition. Antioxidants (Basel, Switzerland). 2023; 12: 1059. https://doi.org/10.3390/antiox12051059.

[27] Carota G, Di Pietro L, Partsinevelos K, Barbati SA, Cardaci V, Graziani A, *et al*. Influence of Oxidative Stress-Mediated Inflammation on the Pathogenesis of Reproductive Disorders: Exploring the Benefits of Carnosine for Prevention and Treatment of Endometriosis. Frontiers in bioscience (Landmark edition). 2026; 31: 45414. https://doi.org/10.31083/FBL45414.

[28] Alhafez M, Kheder F, Aljoubbeh M. Synthesis, antioxidant activity and antibacterial study of EGCG complexes with iron (III) ions. Results in Chemistry. 2022; 4: 100638. https://doi.org/10.1016/j.rechem.2022.100638.

[29] Lu H, Hu H, Yang Y, Li S. The inhibition of reactive oxygen species (ROS) by antioxidants inhibits the release of an autophagy marker in ectopic endometrial cells. Taiwanese journal of obstetrics & gynecology. 2020; 59: 256–261. https://doi.org/10.1016/j.tjog.2020.01.014.

[30] Joseph SK, Sabitha M, Nair SC. Stimuli-Responsive Polymeric Nanosystem for Colon Specific Drug Delivery. Advanced pharmaceutical bulletin. 2020; 10: 1–12. https://doi.org/10.15171/apb.2020.001.

[31] Zhu H, Yang W, Suo Y, Liu Y, Zhan X, Zhou J, *et al*. Nanomaterials engineered for photothermal therapy in neural tumors and neurodegenerative diseases: biomaterial design, clinical mechanisms and applications. Frontiers in bioengineering and biotechnology. 2025; 13: 1631627. https://doi.org/10.3389/fbioe.2025.1631627.

[32] Wang D, Jiang Y, Yang X, Wei Q, Wang H. 6-Shogaol reduces progression of experimental endometriosis in vivo and in vitro via regulation of VGEF and inhibition of COX-2 and PGE2-mediated inflammatory responses. The Korean journal of physiology & pharmacology: official journal of the Korean Physiological Society and the Korean Society of Pharmacology. 2018; 22: 627–636. https://doi.org/10.4196/kjpp.2018.22.6.627.

[33] Nanda A, K T, Banerjee P, Dutta M, Wangdi T, Sharma P, *et al*. Cytokines, Angiogenesis, and Extracellular Matrix Degradation are Augmented by Oxidative Stress in Endometriosis. Annals of laboratory medicine. 2020; 40: 390–397. https://doi.org/10.3343/alm.2020.40.5.390.

[34] Tian YY, Chen LY, Xie FY, Wang J, Xu JH, Li Y, *et al*. Paeonia × suffruticosa Andrews leaves improve endometriosis with anxiety/depression by regulating microglial polarization via JAK2/STAT3 pathway. Phytomedicine: international journal of phytotherapy and phytopharmacology. 2026; 151: 157778. https://doi.org/10.1016/j.phymed.2026.157778.

[35] Xu Y, Liu H, Xiong W, Peng Y, Li X, Long X, *et al*. A novel mechanism regulating pyroptosis-induced fibrosis in endometriosis via lncMALAT1/miR-141-3p/NLRP3 pathway†. Biology of reproduction. 2023; 109: 156–171. https://doi.org/10.1093/biolre/ioad057.

[36] Karakoç E, Koçak SB, Kişifli Köş K, Kayhan H, Erdem Şahinkesen E, Eylem CC, *et al*. Pelargonium graveolens Essential Oil Suppresses Proliferation and Migration and Modulates Mesenchymal-Associated Cellular Functions in Human Endometriotic Cells. Cells. 2026; 15: 702. https://doi.org/10.3390/cells15080702.

[37] Chen Y, Zhang C, Weng X, Jiang S, Cheng B. The impact of near-infrared-triggered photothermal therapy on collagen organization and wound healing. Journal of photochemistry and photobiology. B, Biology. 2025; 272: 113273. https://doi.org/10.1016/j.jphotobiol.2025.113273.

[38] Muraine L, Bensalah M, Butler-Browne G, Bigot A, Trollet C, Mouly V, *et al*. Update on anti-fibrotic pharmacotherapies in skeletal muscle disease. Current opinion in pharmacology. 2023; 68: 102332. https://doi.org/10.1016/j.coph.2022.102332.

[39] Islam MS, Parish M, Brennan JT, Winer BL, Segars JH. Targeting fibrotic signaling pathways by EGCG as a therapeutic strategy for uterine fibroids. Scientific reports. 2023; 13: 8492. https://doi.org/10.1038/s41598-023-35212-6.

Editor's note: The Scientific Editor responsible for this paper were Xiaoyuan Ji and Kelong Fan.

Received: 26th March 2026; **Accepted**: 21st May 2026; **Published**: 26th June 2026